



DEFENSE TECHNICAL INFORMATION CENTER

Information for the Defense Community

Month Day Year

DTIC® has determined on **12 29 2008** that this Technical Document has the Distribution Statement checked below. The current distribution for this document can be found in the DTIC® Technical Report Database.

DISTRIBUTION STATEMENT A. Approved for public release; distribution is unlimited.

© **COPYRIGHTED.** U.S. Government or Federal Rights License. All other rights and uses except those permitted by copyright law are reserved by the copyright owner.

DISTRIBUTION STATEMENT B. Distribution authorized to U.S. Government agencies only. Other requests for this document shall be referred to controlling office.

DISTRIBUTION STATEMENT C. Distribution authorized to U.S. Government Agencies and their contractors. Other requests for this document shall be referred to controlling office.

DISTRIBUTION STATEMENT D. Distribution authorized to the Department of Defense and U.S. DoD contractors only. Other requests shall be referred to controlling office.

DISTRIBUTION STATEMENT E. Distribution authorized to DoD Components only. Other requests shall be referred to controlling office.

DISTRIBUTION STATEMENT F. Further dissemination only as directed by controlling office or higher DoD authority.

Distribution Statement F is also used when a document does not contain a distribution statement and no distribution statement can be determined.

DISTRIBUTION STATEMENT X. Distribution authorized to U.S. Government Agencies and private individuals or enterprises eligible to obtain export-controlled technical data in accordance with DoDD 5230.25.

REPORT DOCUMENTATION PAGE					Form Approved OMB No. 0704-0188	
<p>The public reporting burden for this collection of information is estimated to average 1 hour per response, including the time for reviewing instructions, searching existing data sources, gathering and maintaining the data needed, and completing and reviewing the collection of information. Send comments regarding this burden estimate or any other aspect of this collection of information, including suggestions for reducing the burden, to Department of Defense, Washington Headquarters Services, Directorate for Information Operations and Reports (0704-0188), 1215 Jefferson Davis Highway, Suite 1204, Arlington, VA 22202-4302. Respondents should be aware that notwithstanding any other provision of law, no person shall be subject to any penalty for failing to comply with a collection of information if it does not display a currently valid OMB control number.</p> <p>PLEASE DO NOT RETURN YOUR FORM TO THE ABOVE ADDRESS.</p>						
1. REPORT DATE (DD-MM-YYYY) 31/12/2007		2. REPORT TYPE Final Technical Report		3. DATES COVERED (From - To) 05/01/2006-10/30/2007		
4. TITLE AND SUBTITLE Framing Camera Improvements and Hydrodynamics Experiments			5a. CONTRACT NUMBER N00173-06-1-G906			
			5b. GRANT NUMBER BAA 67-05-01			
			5c. PROGRAM ELEMENT NUMBER			
6. AUTHOR(S) R. Paul Drake			5d. PROJECT NUMBER			
			5e. TASK NUMBER			
			5f. WORK UNIT NUMBER			
7. PERFORMING ORGANIZATION NAME(S) AND ADDRESS(ES) University of Michigan 1058 Wolverine Towers 3003 S. State Street Ann Arbor, MI 48109-1274				8. PERFORMING ORGANIZATION REPORT NUMBER DRDA#06-3311/F015351		
9. SPONSORING/MONITORING AGENCY NAME(S) AND ADDRESS(ES) Naval Research Laboratory Code 6731 Bldg. 101A Room 1100 Washington, DC 20375-5326				10. SPONSOR/MONITOR'S ACRONYM(S)		
				11. SPONSOR/MONITOR'S REPORT NUMBER(S)		
12. DISTRIBUTION/AVAILABILITY STATEMENT Unlimited						
13. SUPPLEMENTARY NOTES						
14. ABSTRACT See attached report						
15. SUBJECT TERMS						
16. SECURITY CLASSIFICATION OF: a. REPORT		17. LIMITATION OF ABSTRACT N/A		18. NUMBER OF PAGES 16	19a. NAME OF RESPONSIBLE PERSON R. Paul Drake 19b. TELEPHONE NUMBER (Include area code) 734-763-4072	

Research Proposal

BAA 67-05-01, Sub-Topic 2

Contract # N00173-06-1-G906

Dates 5/1/2006-10/30/2007

Framing Camera Improvements and Hydrodynamic Experiments

Principal Investigator:

R. Paul Drake,
University of Michigan

December 31, 2007

20081229009

ABSTRACT

We have newly completed a MicroChannel Plate (MCP) evaluation system, in addition to our existing large-MCP mounting system. We developed an improved computational model and conceptual understanding of MCP performance. We also propose to participate in hydrodynamic experiments at NRL whenever they occur, to prepare for an experiment for NIKE to study the onset of turbulence via the Kelvin Helmholtz instability, and if circumstances permit to conduct such an experiment.

1. INTRODUCTION

We have been training a graduate student, Eric Harding, in areas relevant to x-ray diagnostics of interest to NRL and to hydrodynamic experiments at NRL. Eric, working with several additional contributors at Michigan and with Jim Weaver of NRL, has greatly improved our x-ray-diagnostic characterization capability. We are now completing a significant upgrade of our hardware capability, described below. In addition, Eric's research and work with more-junior students has continued to lead to improvements in the computational model of MCP performance that he developed. We believe that our ability to analyze and model the behavior of MCPs for analog imaging applications now exceeds the previous state of the art (most previous work is dedicated to pulse-counting applications). This has prepared us to address the optimization of x-ray framing cameras for NRL applications and long-term possibilities for improvements in performance, a process we have begun.

Eric is also now working on the conceptual design of an experiment for NIKE, which he will use in his candidacy exam this winter. His goal is to potentially observe the onset of hydrodynamic turbulence from a shear flow in a high-Mach-number, high-energy-density system. Such an observation would be new and would have important consequences in both the laboratory and astrophysics. The current state of the experiment design is described in the following. Eric is scheduled to assist in upcoming hydrodynamic experiments by NRL scientists on NIKE and we propose that this continue.

2. RECENT AND PROPOSED RESEARCH

The recent research of our group provides the basis for the activities we propose. Here we discuss key results related to x-ray characterization hardware, framing camera modeling, and the conceptual design of an experiment. This work has been supported primarily by NRL. Significant additional support has been provided by the University of Michigan, which has supported the activity of several undergraduate students and some graduate-student effort, and by the National Science Foundation through the Research Experience for Undergraduates program.

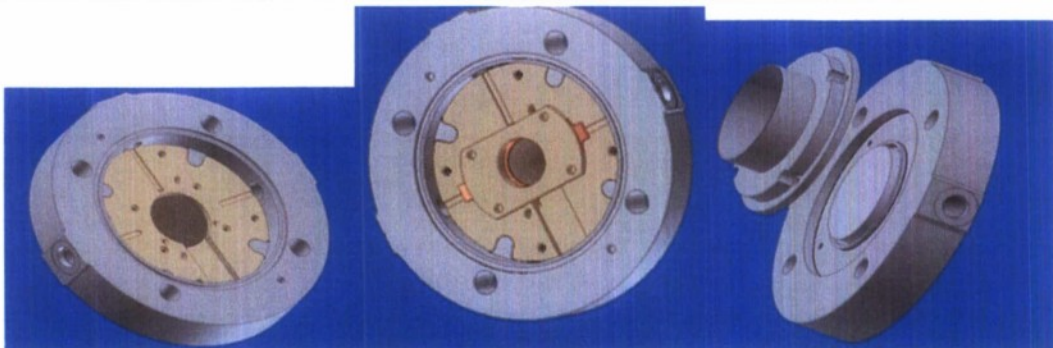


Figure 1. CAD images of the MCP evaluation system. From left to right, these show the housing that holds the entire assembly and provides the seal to the vacuum system, the reflecting grid support system which supplies voltage to both the MCP and reflecting grid and maintains even pressure on the MCP, and the fiber optic faceplate retention system which seals the faceplate to the housing and provides a light tight seal to the lens and CCD.

A. MCP Evaluation System

We have designed and built a system for mounting and testing one-inch diameter MCPs, with the goal of evaluating a number of options for improvements to MCP performance. The point of using one-inch MCPs for such studies is that they are a great deal less expensive than the two-inch plates. The design was primarily the work of second-year graduate student Tony Visco, using the 3D CAD program Inventor. Such a design must meet some demanding engineering constraints. It must create a good vacuum seal at the edges of the fiber optic faceplate, yet must not obscure this plate and must keep the phosphor surface of the faceplate at a very precise distance from the MCP surface. The MCP must be held without undue stress. Voltage must be supplied, via vacuum feedthroughs, to the MCP and the phosphor. It is useful to make certain distances adjustable. The distance between the MCP and the fiber optic faceplate can be varied between 250 μ m and 750 μ m. Smaller separation distances provide better image resolution for a given voltage, but reduce the maximum voltage that can be applied to the fiber optic plate due to greater chances of electrical arcing. In addition, to test the benefits from re-injecting those electrons that leave the front surface of the MCP, one needs to be able to support a grid above the MCP and to provide voltage to the grid. The distance between the reflecting grid and MCP is also variable, allowing for experimental determination of separation and potential differences that will optimize the detection efficiency of the MCP. Figure 1 shows some images from the CAD design.

Figure 2 shows the assembled system. It has 65 parts including 26 springs and screws. The machined parts were produced in our machine shop, and our spaceflight-certified technicians did the soldering. At this writing the unit has been vacuum tested. In contrast to the mounting system for two-inch plates that was donated by LLNL, no leaking could be detected down to the base pressure of the vacuum system, which was 3.7×10^{-7} Torr. In addition, high-voltage tests have shown that the unit holds voltage to design values using an uncoated fiber-optic faceplate. The faceplate has now been sent out for coating. By the time the proposed contract would begin, we expect this system to be operating.



Figure 2. Photographs of the assembled MCP evaluation system. The left photograph shows this system attached to our vacuum system. The three vacuum feedthroughs supply voltage to the phosphor faceplate, MCP and reflecting grid. The right picture shows the MCP holder and grid supports system contained within the housing. The separation distances between faceplate and MCP and between the MCP and reflecting grid can be varied while maintaining an even pressure by use of a spring suspension system.

In addition, our two-inch mounting system remains available for measurements using larger MCPs, when needed. As one example, we have obtained two sample MCPs in this size with square pores. These may potentially have lower noise than MCPs with round pores do because they have a uniform angle-of-incidence for x-rays onto the channel wall. Moreover, the two-inch mount will be important to characterize MCPs that are intended for use on framing cameras at NRL.

We can make several measurements with either of these mounting systems. Because we simultaneously measure the absolute flux of x-ray photons, we can analyze all the measurements in terms of the absolute number of incident photons. The most informative measurement may be the "starry sky" image in which we operate the MCP at fairly high gain to observe the distribution of signal amplitude. This has distinct meaning because different levels of signal arise from the interaction of x-rays with different portions of the MCP pore, as is discussed further below in the context of our MCP model. Figure 3 shows such an image. A second type of measurement we can

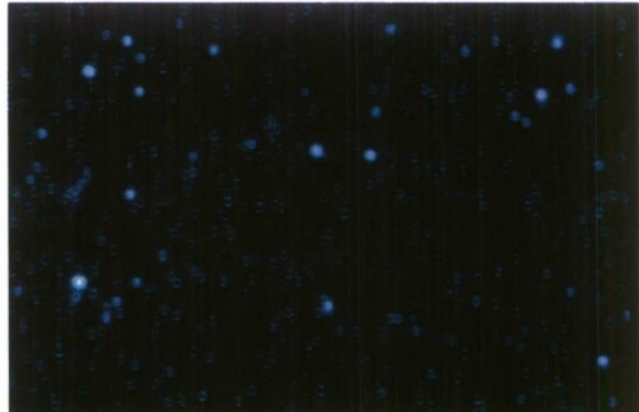


Figure 3. Single-photoelectron events detected with our x-ray system. The data have been processed using a star-finder program adapted by Eric Hardling. This produced the circles on the plot, which are also present for the bright dots but do not show up on this display. The measurement used a 2 inch diameter MCP. It has a CsI photocathode coating to a depth of 1.5 pore diameters. The MCP properties were: pore diameter 10 μm , thickness of MCP 600 μm , bias angle 8 degrees, and applied voltage 1150 V. The x-ray properties were: energy 1.49 keV (Al K α), 0.016 average incident photons entering each MCP pore, 500 events found, $\delta G/G \sim 1.5$, quantum efficiency 39%.

make is a statistical measurement that determines the “Detected Quantum Efficiency” as was done by Pawley *et al.* [1]. This has contributions relating to the distribution of secondary electron yield produced by incident x-ray photons on various parts of the MCP pore and also has contributions from the gain variation in the system, as we have discussed in previous reports to NRL. Third, by obtaining very long exposures, we can quantify the “fixed pattern noise” believed to be due primarily to variations in phosphor gain. Fourth, either by measuring the structure of the dots in the starry sky image or by using a knife-edge, we can determine the point spread function and thus the resolution of the system that includes the MCP. We expect to make initial measurements with the new one-inch system during early 2006.



Figure 4. Newly designed x-ray photodiode mount and Be filter cover.

B. Other Improvements To The X-Ray Characterization System

We have continued to make operational improvements to the x-ray system used for the measurements discussed above. We reworked the anode shield on our x-ray source to allow the installation of various filter assemblies and pinholes. We have also designed and built a new photodiode mount with an improved vacuum feedthrough (See Figure 4). The assembly allows a wide variety of filters to be placed in front of the photodiode, while maintaining a light tight enclosure. This has allowed an undergraduate student to measure the x-ray flux through a number of filters, including polymer based filters, such as polystrene, which would melt if fixed to the x-ray anode shield. He also wrote some software based on published methods to deconvolve the x-ray spectrum from such K-edge spectroscopy measurements. This work is continuing, and is intended to place limits on the x-ray flux that is in energy bins other than that of the K_{α} line the source is intended to produce. Another of our undergraduates did a project to measure the gain and linearity of an inexpensive (< \$1000) intensifier, which provides another possible option for boosting the sensitivity of the detection of weak single-photon events. She found that the gain was approximately 4x and that the amplification was linear over the range tested.

C. Framing Camera Modeling

It has been the point of view of the community using microchannel plates (MCPs) for analog imaging that the primary factor limiting the performance of these devices has been the quantum efficiency. Here, quantum efficiency is defined as the fraction of incident photons that produce signal in the detector. This point of view has been supported by a number of measurements reported in the literature [1-5] that seem to indicate a quantum efficiency in the range of 1 to 10%. In particular, this was the result that Carl Pawley obtained at NRL by statistically measuring the Detected Quantum Efficiency (DQE) of

an MCP with a gold photocathode (created when “striplines” were laid down to allow gating of the plate). A standard framing camera at present achieves a DQE that is far below the potential maximum value. The conclusion is that the noise introduced by framing cameras might be greatly reduced by improved design.

An important point is that a measurement seeking to determine an averaged quantum efficiency by statistical means must operate with a low photon flux, so that the Poisson statistics of the output is determined by the limited number of detected events. This led us to seek to measure single-photoelectron events and to emphasize “starry sky” images. Examination of these images in turn led us to think in more detail about the process by which the signal is generated. We have described this in detail in previous reports to NRL, and will only summarize it here, with reference to Figure 5.

Some incident x-rays strike the “webbing” between the channels, producing almost no signal in present applications. Those that do enter the (circular) pores strike the surface of the pores at variable angles of incidence, with the angle from the surface ranging from 0 degrees to the bias angle (θ). In addition, some of these x-rays strike the photocathode material while others penetrate further and strike the bare glass interior surface. The x-rays at any given angle produce a Poisson distribution of secondary electron yield, whose mean value is strongly sensitive to both the value of the angle of incidence and to the material they encounter. On a fresh CsI surface and at an optimum angle, the total yield of secondary electrons can exceed 20. These secondary electrons are then accelerated down the pore and are multiplied by secondary electron emission during successive collisions with the wall of the pore, producing a cloud of electrons that eventually emerges from the rear of the MCP. The number of electrons produced by a single x-ray photon depends on more than the number of secondary electrons initially produced. The average gain for these electrons decreases when they are produced deeper down the channel, as they then undergo less successive bounces through the remainder. (The gain of photons striking at the same depth is also variable, with a statistical distribution about some typical value, but this is a comparatively small source of noise and we have not addressed it in modeling as yet.)

These considerations led Eric Harding to develop a Monte Carlo model of a single MCP pore. We have described the model and its first results in previous reports to NRL. A paper reporting these first results is awaiting the comparison with a bit more laboratory data with newly coated MCPs (and was eventually published in Rev. Sci. Instr.). More recent modeling work has focused on some aspects of MCP behavior not included in the initial model. Our primary work in this area has been motivated by a paradoxical aspect

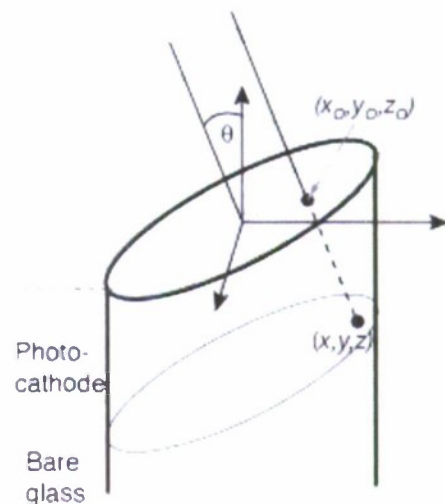


Figure 5. Geometry used for simulations. The MCP bias angle is θ . The channel mouth coordinates of an incident photon are (x_0, y_0, z_0) . The coordinates of a photon strike on the channel wall are (x, y, z) . Note that the channel mouth is an ellipse and photon path is normal to the ellipse plane

of the standard view of these MCPs. The pore is typically coated for a distance of about 1 to 1.5 pore diameters with a "photocathode" material, such as gold or CsI, or with nichrome to less depth on a "bare" MCP. If a non-conducting photocathode material such as CsI or KBr is used, a conducting material such as gold or nichrome must be applied as an undercoat, so the MCP can still be biased. The notion is that these applied materials will produce more secondary electrons than bare glass, and as a result will produce more signal. However, the conducting layer, which may also be playing the role of a photocathode, maintains the coated section of the pore at a constant electric potential. In addition, observations show that electrons incident on surfaces such as MCP glass at low energy produce negligible electron yield. As the electron energy approaches 30 eV (also known as the "first cross-over potential"), the average yield, which includes both backscattering and the release of electrons from the material, increases rapidly to unity. The yield increases above unity at higher energy. It seems that the secondary electrons produced in the conducting photocathode section, with energies of a few eV, will most likely drift across into the opposing pore wall with insufficient energy to create significant electron yield. Some secondary electrons may drift out the mouth of the pore into vacuum and be lost. Of those secondary electrons that do drift down the pore, where they might potentially be amplified, it seems that only a small fraction are likely to enter the strong field region on a trajectory that lets them be accelerated past the first cross-over potential. Thus, an interesting question is what fraction of those photocathode electrons that do drift down the pore end up producing signal, and how much signal they do produce. In addition, if one were to use a reflecting grid, one would like to know what fraction of the re-injected electrons ought to produce usable signal within the gating time.

We are addressing this question through modeling of the electric potentials and electron optics in the pores, being carried out by an undergraduate student under Eric's supervision. Initial modeling with software written in IDL showed that it was necessary to model an extended array of pores in order to accurately calculate the electric field. To do this well and to model the electron behavior in the fields accurately, we began working with some (rather expensive) commercial software that we are now using on a lease-to-own basis. So far we have been able to accurately solve the electric field inside a pore. The goal is to build a quantum efficiency map of the pore surface by simulating the release of secondary electrons (in actual MCP operation these are released from the absorption of incident x-rays, but in the present simulations we are not concerning ourselves with the x-ray/material interactions) from different regions of the pore wall near the input of the pore, and then tracking the electron's energy as it moves through the electric field. If the electron strikes the adjacent pore wall with energy greater than the first cross-over potential, we say we have a quantum efficiency of 1, while if the energy is less the first cross-over potential, we say we have a quantum efficiency of 0. This process will be repeated 100 times per differential area element of the pore wall in order to build up a map of the entire surface that would be seen by incoming x-ray photons. We can then incorporate the results of these simulations into the MCP output model. To do so, we will multiply the total number of secondary electrons emitted from an area element (due to an incident x-ray) by the quantum efficiency for the subsequent generation of an electron corresponding to that element, in order to get the number of secondary electrons that actually participate in producing an output signal. We plan to

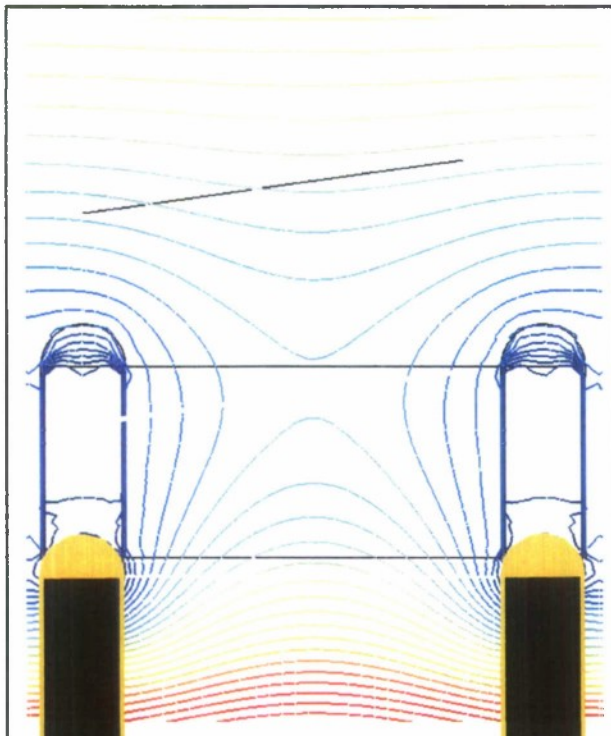


Figure 6: Voltage contour plot of the input end of a MCP pore with a $10\mu\text{m}$ diameter. The grey shaded regions represent the MCP glass walls, the yellow regions are the electrodes that are held at a negative voltage to the glass. In this particular simulation, the electrode is Ni and extends down the pore. The input electrode is held at a constant -900V while the output electrode is grounded. The software package LORENTZ-2D from Integrated Engineering Software was used to perform this simulation.

first do these simulations in 2-dimensions and then eventually in 3-dimensions. Figure 6 shows a voltage contour plot at the input end of a pore, from a 2D simulation.

If indeed it turns out, as seems likely at present, that only a small fraction of the electrons from the photocathode are now further amplified, then one could consider making changes in the MCP structure to address this. For example, one could build an MCP with embedded conducting layers that would enable one to tailor the electric field profile and in particular to accelerate all the electrons emerging from the photocathode region to useful energies.

We propose to continue with modeling research aimed at improving the Monte Carlo model. This research will be under Eric's supervision and carried out primarily by undergraduate students, often funded by fellowships or other support, or by new graduate students as preliminary projects. Our goal is to make steady progress in our ability to model MCP-based framing cameras, and in the process to identify

approaches to improving MCP and framing camera performance. We anticipate that this work will lead to a sequence of publications exploring various aspects of the use of framing cameras for analog imaging. We intended to investigate the differences in electric field interaction with secondary electrons between circular and square pore MCPs. We also intended to investigate the variation of MCP output signal with variations in MCP bias angle and photocathode coating depth.

D. Experimentation on NIKE

Eric Harding spent time at NIKE during the present contract, in order to learn from assisting with hydrodynamic experiments. He also actively worked on the physics design of an experiment that could be done on NIKE. The physics design as now conceived is discussed next, although as always it may evolve significantly as it proceeds.

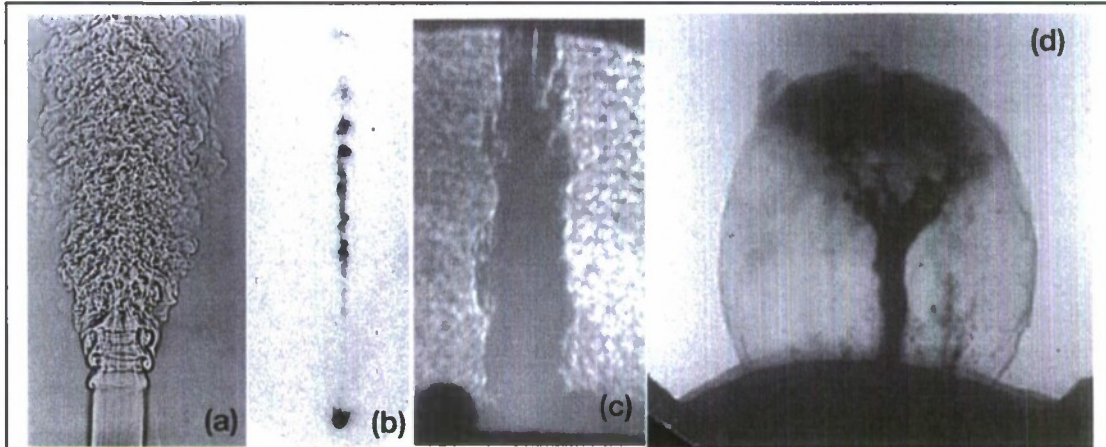


Figure 7. Comparison of various jets. (a) Shadowgraph visualization of subsonic jet in gas, from Van Dyke Album of Fluid Motion (1982). (b) The jet in HH34, obtained by WFPC2 on the Hubble space telescope. (c) Jet produced in a z pinch, by Lebedev *et al* [6] (d) Jet produced in a laser experiment by J. Foster and the Omega Jet Team. In this specific case there is some possibility that surface tension plays a role, but other hotter jets in the same experiments also show no KH.

The problem of interest, broadly speaking, is the onset of hydrodynamic turbulence in high-Mach-number shear flows. This is motivated by the following observations. In subsonic laboratory experiments or natural fluid systems shear flows of sufficiently high Reynolds number Re ($> 10,000$) often rapidly develop into a turbulent state. The development proceeds from the Kelvin-Helmholtz (KH) instability through one or more secondary instabilities to a final state featuring a high level of vorticity across a large range of spatial scales, and characterized by the rapid, diffusive interpenetration of each material into the other. Numerical simulations cannot reproduce this behavior, because their numerical viscosity limits Re in their calculations to $\sim 1,000$. Yet shear flows of very high Re and very high Mach number play an important role in a wide range of physical systems, from combustion engines for scramjet propulsion to the evolution of supernovae. This makes it natural to wonder whether the extensive material mixing observed in typical laboratory environments also occurs in astrophysics. One sees that such mixing does not occur in supersonic astrophysical or laboratory jets [7], which form a bow shock that surrounds the jet with a “cocoon” of material at an intermediate velocity, and which apparently develop a gradual enough gradient in the velocity profile to avoid the initial onset of the Kelvin-Helmholtz instability that would begin the sequence leading to turbulence along the stem of the jet. Figure 7 illustrates this. Yet there are many other environments, including winds blowing across disks, the surfaces of Rayleigh-Taylor spikes in supernovae, and flowing plasmas in high-energy-density experiments, in which there is no cocoon. In this context, the question is whether one can produce a high-Mach-number, abrupt shear layer that should produce so much Kelvin-Helmholtz growth that subsequent processes are likely to develop, in a diagnosable environment. This is the focus of the current design effort

A variety of high-Mach-number, shear-layer experiments, with $Re \sim 10^4$ to 10^5 cm^{-1} have been performed with typical gases such as air, helium, and nitrogen in supersonic wind tunnels [8-11]. A typical experimental geometry is shown in Fig. 8.

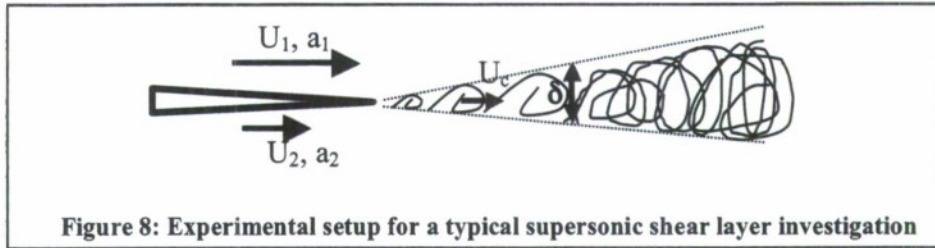


Figure 8: Experimental setup for a typical supersonic shear layer investigation

Most previous high Mach number experiments have had internal Mach numbers $M_1 = U_1/a_1$ and $M_2 = U_2/a_2$ between 1 and 4. The free stream velocities are measured using pressure transducers. These experiments show marked decrease in growth rate of the mixing layer (δ) for a range of convective Mach numbers, M_c , where M_c is defined by Eq. 1 as

$$M_{c1} = \frac{U_1 - U_c}{a_1} \quad , \quad [1]$$

$$M_{c2} = \frac{U_c - U_2}{a_2}$$

where U_1 and U_2 are the free stream velocities of the two fluids with sound speeds a_1 and a_2 and U_c is defined as the convection speed of the large-scale flow structures. A related intermediate velocity that can be defined in advance of having data is $U_o = (U_1 + U_2)/2$, the average velocity of the two fluids. M_c is an important non-dimensional quantity because it is calculated in a frame that is relevant to the internal flow dynamics. It is related to compressibility effects in the shear layer, which have been shown to decrease the mixing-layer growth rate. Papamoschou and Roshko have shown experimentally a factor of 4 decrease in mixing-layer growth rate for $M_c = 1$ compared to a subsonic flow [10]. These flows are typically observed far enough from the splitter plate that the flow has become fully turbulent. This is comparatively far as $U_o > U_2 > a_2$. In this mode, using Schlieren photography, one typically sees a fully developed mixing layer with some large-scale structure (See Fig. 9)

In our high-energy-density (HED) systems, which we use in experiments on Omega to experimentally model a supernova, the upstream Mach numbers range from 50 to 100,

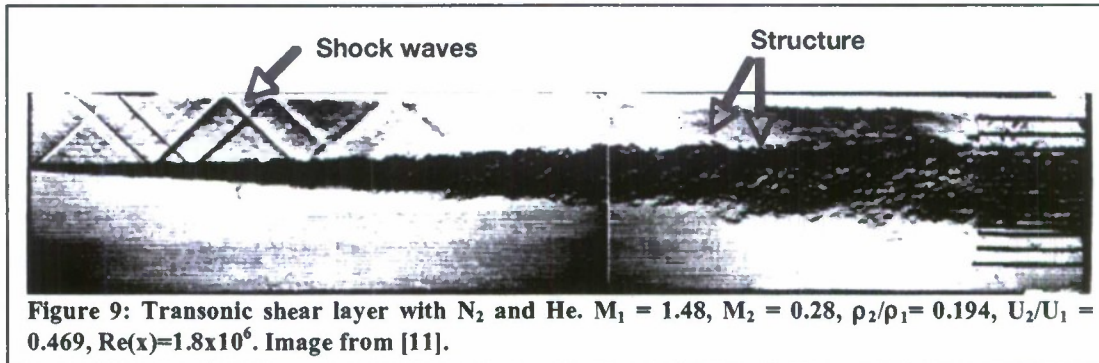


Figure 9: Transonic shear layer with N_2 and He . $M_1 = 1.48$, $M_2 = 0.28$, $\rho_2/\rho_1 = 0.194$, $U_2/U_1 = 0.469$, $Re(x) = 1.8 \times 10^6$. Image from [11].

but we have yet to observe a fully turbulent flow. Before a flow like that shown in Fig. 8 goes turbulent there is a small region, near the tip of the splitter plate, where the flow is laminar. This laminar layer quickly develops Kelvin-Helmholtz roll ups, which soon go turbulent due to the high Reynolds number of the flow. The question for our proposed experiment is whether and how far we can drive the evolution from the Kelvin-Helmholtz toward a turbulent state in a focused HED experiment.

When thinking of creating a velocity shear layer, a high Mach number jet appears to be a good choice. However, as we discussed above the development of a cocoon apparently is related to the absence of KH in such systems. This leads us to focus on experimental approaches that do not produce a bow shock.

From, simple linear theory (neglecting viscosity) the KH growth rate is given by

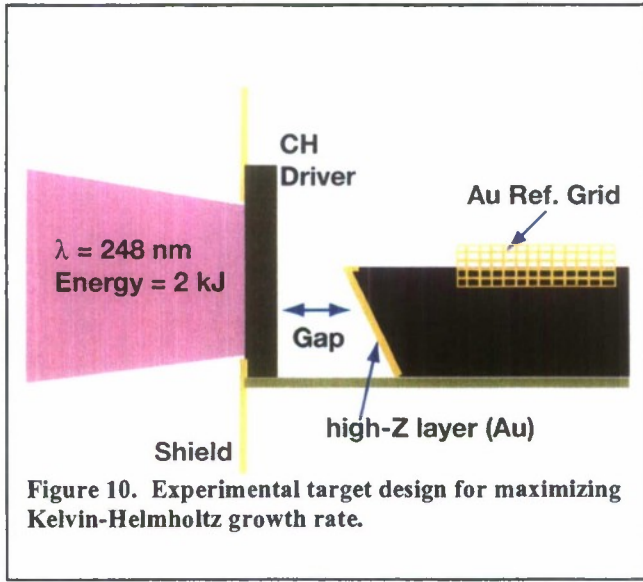
$$n = k(U_2 - U_1) \frac{\sqrt{\rho_1 \rho_2}}{\rho_1 + \rho_2} \quad [2]$$

where k is the instability wavenumber and ρ_1 and ρ_2 are the fluid densities. This growth rate is maximum for equal densities. It decreases only slowly as the densities become unequal, dropping less than a factor of 2 for tenfold differences in density. Thus, in our proposed experiment we aim to maximize the velocity shear between two fluids with equal densities.

Figure 10 shows a diagram of one possible target geometry. The laser beams strike the “driver”, a plastic layer intended to act both as an ablator and a working material. A gold shield prevents the outer edges of these beams from interfering. The driver is separated by a gap from a gold flow-splitter. The gold splitter slices off the flowing plasma of interest, diverting the flow beside it. The layer of gold is thick enough to delay the shock through the gold until after times of interest. The flow of interest proceeds across the SiO_2 foam surface, at a pressure of about a Mbar. This drives a shock down into the foam, converting the foam into plasma without imparting significant lateral motion to it. The two fluids then interact across a steep shear layer, which should drive Kelvin-Helmholtz and subsequent effects. The Au grid allows calibration of location and magnification. The scale of the target is optimized for the NRL NIKE laser parameters, listed in Table 1.

Nominal Drive Beam Energy	2 kJ
Laser Spot Size	750 μm (FWHM) 400 μm (flat top)
Pulse Length	4 ns
Wavelength	0.248 μm
Max. Backlighter Delay	8 ns

Table 1. NIKE operational parameters



To determine the viability of an experiment, one needs to determine how strongly one can drive Kelvin Helmholtz growth. We will use the total number of linear-regime e-foldings as an indicator of this. This number is the growth rate from Eq. 2 times the duration of the useful flow, when observed in the mean-flow frame. This time is roughly the ratio of the length of the flowing plasma that is at a high enough density to produce significant growth to the mean-flow velocity. The specific design parameters for this target include

how thick to make the driver, how large to make the gap, what density to make the foam, and what materials to use to allow radiographic diagnosis.

We used the Hyades simulation code, a Lagrangian, one-dimensional, single-fluid three-temperature radiation-hydrodynamics code with a good laser-absorption model, flux-limited-diffusion electron-heat transport, and multigroup-diffusion radiation transport, to model this system. In doing so, we use a laser irradiance that is 1/3 the nominal value, as experience has shown that this is necessary in 1D codes to compensate for the actual loss of heat through radial heat transport. The behavior is only moderately sensitive to the exact irradiance, so questions of whether this factor should be 25%, 33%, or 40% for 248 nm light are not important during the design phase.

Figures 11, 12, and 13 show the density and velocity profiles for Hyades runs with 20, 50, and 100 μ m CH drivers using Table 1 parameters, at several different times in each case.

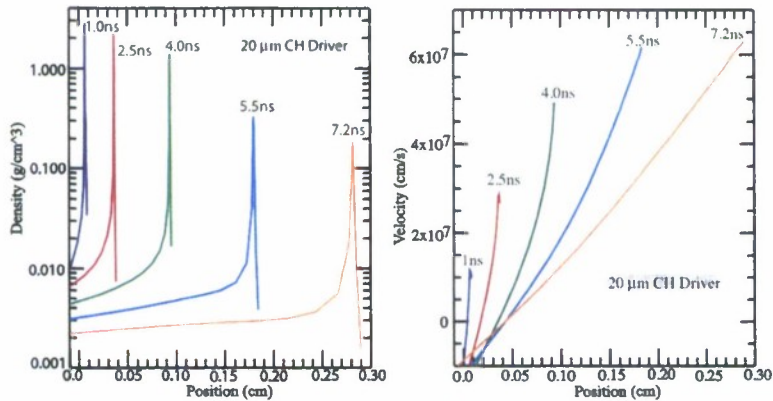


Figure 11. 20 μ m driver

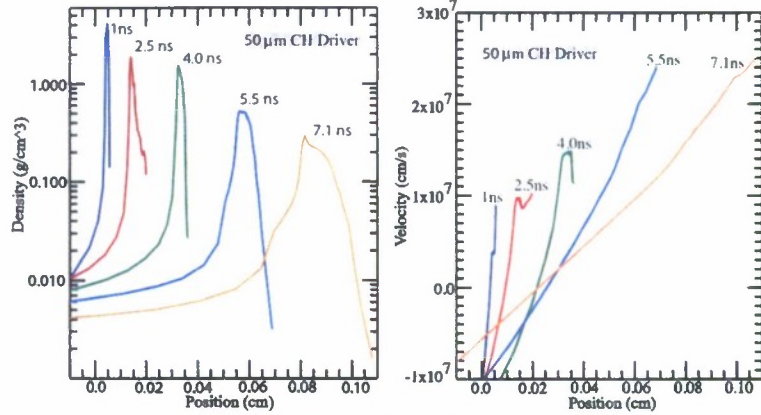


Figure 12. 50 μ m driver

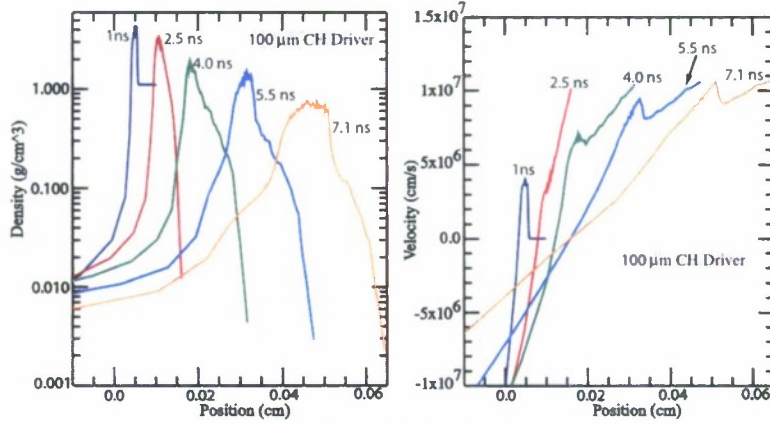


Figure 13. 100 μ m driver

Assuming a diagnostic resolution of 10 μ m we would hope to observe 100 μ m KH structures. In terms of the above parameters, $U_2 = 0$ here. With $U_1 = 100$ km/s ($= 10^7$ cm/s on the graphs and also $= 100$ μ m/ns), and $\rho_1 = \rho_2$ one finds a KH growth rate $n \sim 3$ ns⁻¹.

In these simulations, the 50- μ m thick driver appears optimum. It gives a fairly smooth plasma profile and the longest slug of plasma moving at ≥ 100 km/s. This is ~ 400 μ m at a distance near 1 mm, with a density within a factor of 10 of the nominal 100 mg/cc foam density. In the mean flow frame, at ~ 50 km/s, the 400 μ m slug of plasma moves by in 8 ns. This is well matched to the NIKE timeframe and would produce roughly 24 linear e-foldings, which is very far into the nonlinear regime. The pressure in the slug of plasma is about 1 Mbar. Its sound speed a_1 is about 35 km/s, so the ratio $U_0/a_1 \sim 1.5$. The sound speed a_2 of the shocked foam material will be about 17 km/s, making U_0/a_2 larger than U_0/a_1 . The shock speed in the foam under these conditions is approximately 30 km/s, so that a layer of fluid ~ 100 μ m thick is available to interact with the flowing driver plasma. Using a lower-density foam is an option that would produce a thicker fluid layer with a higher sound speed.

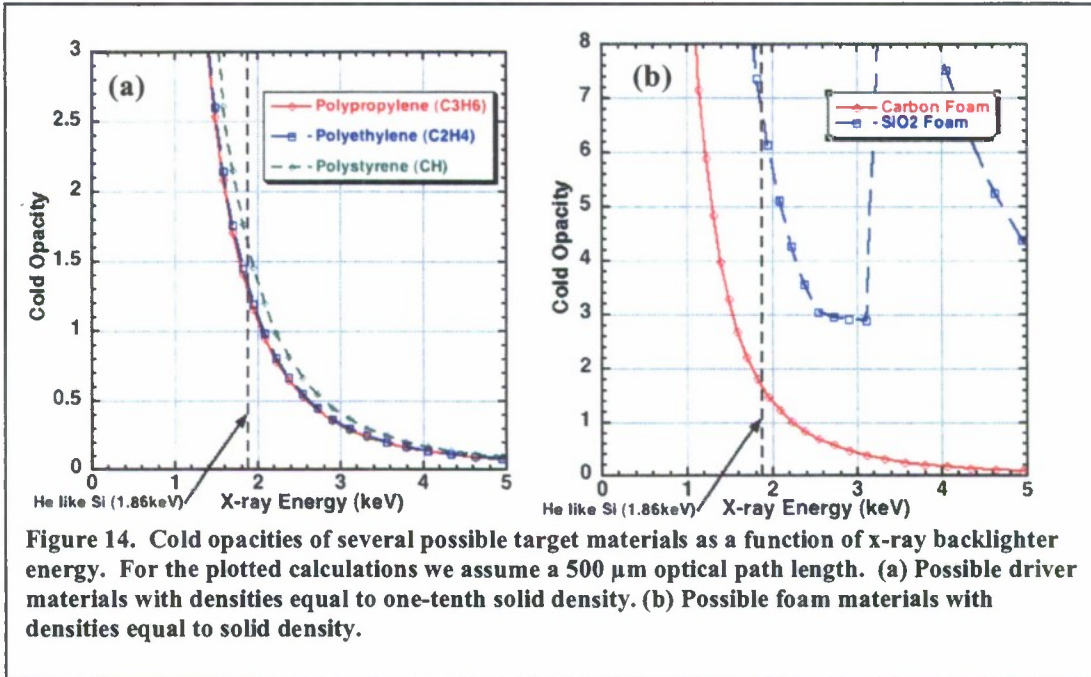


Figure 14. Cold opacities of several possible target materials as a function of x-ray backscatterer energy. For the plotted calculations we assume a 500 μm optical path length. (a) Possible driver materials with densities equal to one-tenth solid density. (b) Possible foam materials with densities equal to solid density.

Upon closer examination, one can see that this driver thickness allows for the driver to be shocked throughout, for the rarefaction wave to move back to the front surface, and for the driver to be reshocked into a thin, dense layer before the laser shuts off. After this the dense layer drifts and expands, providing a smoothly varying density. In contrast, the 100-micron driver appears to be slower and denser than would be optimum. The 20- μm driver has been recompressed and strongly accelerated so that in 1D it appears as too thin a layer to be useful. In actuality, such a target would quite possibly be torn apart by Rayleigh-Taylor instabilities during acceleration.

Target Diagnostics

To capture high-resolution 2D spatial radiography of our target we intend to use spherical crystal imaging and a gated x-ray framing camera with a Si backscatterer (1.86keV). Other backscatterer options could include H like Mg (1.48keV), Fe, and Ti. As a rough rule of thumb we are aiming for a maximum of 1.5 to 2 optical depths in the hot driven plasma, so we can observe structure within it, and a higher optical depth in the foam to achieve the desired contrast between the two materials. From simulations we expect the plasma density of the laser driven material to be around 0.100 gm/cm³ during the time of interest. Given that the footprint of the drive beams is 0.4 mm in diameter, we are expecting to diagnose a plasma with an optical path length around 0.5 mm. We assume during the time of interest the foam, which has been shocked by the expanding driver material, is at a density equal to or greater than its initial density. In contrast, the driver material has expanded and cooled to approximately one-tenth its initial density by the time it interacts with the foam. In Figure 14, the optical depth, which in this case is the product of the mass absorption coefficient, material density (in gm/cm³), and optical path length (taken as 500 μm), is plotted against x-ray backscatterer energy. Using cold opacities in assessing these materials is reasonable because the backlighting photon energy is large compared to

the energy associated with the atomic structure of the plasma ions at the temperatures present here. Looking at Figure 13, a CH (polystyrene) driver illuminated by 1.86keV x-rays has an OD equal to 1.5, while a SiO_2 foam has an OD close 7. These numbers fit fairly well with our design parameters. Due to the high OD of the foam, we will probably be unable to resolve internal structure of the foam as it becomes entrained into the driver material.

References

1. C.J. Pawley and A.V. Deniz, Rev. Sci. Instrum., **71** (2000)1286
2. O.L. Landen, et. al. Rev. Sci. Instrum., **75** (2004) 4037
3. K. McCammon, et. al, Ultrahigh Speed and High Speed Photograph, Photonics, and Videography '90, SPIE vol. **1346** p.398.
4. J.D. Wiedwald et. al. Ultrahigh Speed and High Speed Photograph, Photonics, and Videography '90, SPIE vol. **1346** p.449.
5. D.G Sterns, J.D. Wiedwald, B.M. Cook, R.L. Hanks, and O.L. Landen, Rev. Sci. Instrum. **60** (1989) 363
6. S.V. Lebedev, J.P. Chittenden, F.N. Beg et al., Laboratory astrophysics and collimated stellar outflows: the production of radiatively cooled hypersonic plasma jets, *ApJ* **564**, 113 (2002).
7. R.P. Drake, Hydrodynamic instabilities in astrophysics and in laboratory high-energy-density systems, *Plas. Phys. Contr. Fusion* **417**, B419 (2005).
8. D. Papamoscho, Structure of the Compressible Turbulent Shear Layer, AIAA-89-0126, 27th Aerospace Sciences Meeting, January 9-12.
9. P.E. Dimotakis, Entrainment into a Fully Developed, Two Dimensional Shear Layer. AIAA-84-0368, 22nd Aerospace Sciences Meeting, January 9-12.
10. D. Papamoscho and A. Roshko, Observations of Supersonic Free Shear Layer, AIAA Paper 86-0162, Jan. 1986.
11. J.L. Hall, P.E. Dimotakis and H. Rosemann, Experiments in Non-Reacting Compressible Shear Layers, AIAA-91-0629, 29th Aerospace Sciences Meeting January 7-10.